PROCEEDINGS, 50th Workshop on Geothermal Reservoir Engineering
Stanford University, Stanford, California, February 10-12, 2025
SGP-TR-229

# Application of Strain Transfer Model for Fracture Conductivity Modeling and Monitoring of Enhanced Geothermal Systems.

Queendarlyn A. Nwabueze and Smith Leggett

Bob L. Herd Department of Petroleum Engineering, Texas Tech University, 807 Boston Avenue, Lubbock, TX 79409-3111

qnwabuez@ttu.edu

**Keywords:** Strain transfer model, Fracture width, Flow circulation area, Flow circulation volume, tracer tests

## ABSTRACT

Monitoring geothermal reservoirs using fiber optics is crucial for optimizing fluid circulation and understanding fracture conductivity within the subsurface. The efficiency of optical fiber sensors in detecting geothermal reservoir strain distribution heavily depends on the quality of bonding between the formation and the fiber. Intermediate layers between the geothermal formation and the fiber core can alter strain measurements. This study aims to enhance the accuracy of strain-based measurements in enhanced geothermal systems (EGS) by applying a strain transfer model. In this research, we adopt an existing strain transfer model used in concrete structures to address interfacial slip and variations in the elastic properties of multilayer systems. We integrate this model with a linear elastic fracture model that accounts for the rock strain during fluid. This integrated model improves monitoring in multilayer well completions by effectively transferring strain from geothermal fractures to fiber optic sensors.

Our model demonstrates that fracture width, fracture conductivity, the strain-lag parameter, and rock mechanical properties significantly influence the strain distribution induced by geothermal fractures. The model interprets strain variations caused by changes in hydraulic conductivity, driven by pressure and temperature fluctuations during fluid circulation. The strain-lag parameter illustrates the delayed response between the induced strain and actual fracture deformation, particularly in regions with variable fracture conductivity. These insights are crucial for identifying high-conductivity fractures that control fluid movement between wells, thereby enhancing thermal recovery of the enhanced geothermal system. This work introduces a new application of the strain transfer model to improve fiber optic-based strain measurements in EGS, contributing to the optimization of fluid circulation and better reservoir characterization. By incorporating fiber optic strain measurements, we gain a detailed understanding of fracture conductivity, which is essential for maximizing energy production in geothermal reservoirs.

## 1. INTRODUCTION

Geothermal energy production depends on the flow circulation area available for heat exchange (Ren et al., 2023). Direct measurement of the flow circulation area in deep geothermal reservoirs is impractical, requiring alternative estimation methods (McCabe et al., 1983). Tracer tests provide one of the most effective methods for evaluating geothermal fluid circulation efficiency, and thermal recovery (Redden et al., n.d.; Shook & Suzuki, 2017; Suzuki et al., 2019). Injecting chemical or thermal tracers into the geothermal reservoir and analyzing breakthrough behavior provides an estimate of the swept pore volume (Ren et al., 2023; Shook & Suzuki, 2017). An estimate of swept pore volume is possible for each fracture when circulation tracer measurements are combined with production and injection logs. The flow circulation area in geothermal reservoirs can be calculated from the subsurface fluid circulation volume and the fracture width according to Equation (1).

$$A_f = \frac{V_f}{w_f} \tag{1}$$

Here, $A_f$ is the fracture flow circulation area, $V_f$ denotes the fracture flow circulation volume and $w_f$ represents the fracture width. Thus, to accurately predict the flow circulation area from tracer test data, an independent estimate of fracture width is essential. Without reliable fracture width estimation, tracer-based interpretations remain incomplete, limiting their effectiveness in geothermal reservoir characterization.

Direct measurement of propped fracture width in multistage fractured wells is challenging. These difficulties have led to the development of indirect estimation methods such as numerical modeling, pressure-based diagnostics, and fiber-optic sensing technologies (Cipolla et al., 2008, 2010). Various methods have been developed to estimate propped fracture width, each with its own advantages and limitations. Analytical fracture mechanics models provide theoretical approximations based on rock elasticity, fluid pressure, and fracture dimensions (Belyadi et al., 2017; Wilson & Landis, 2016). Advanced numerical models incorporate geo-mechanical interactions, stress shadowing, and multiphase flow to improve fracture width predictions (Jung et al., 2016; Mahmoud et al., 2021; McClure Mark et al., 2016). Discrete element method (DEM) and finite element method (FEM) can be used to simulate stress-induced changes in the fracture width (Wang & Sharma, 2018). A study showed that optimizing fracture width based on strain simulations enhances conductivity and production efficiency (Rahman et al., 2012). Micro-seismic monitoring offers valuable geometric constraints but lacks the resolution to measure local fracture aperture variations (Le Calvez et al., 2005; Ou et al., 2022). More recently, distributed strain sensing (DSS) using fiber-optic cables has become a viable tool for real-time fracture diagnostics (Jin et al., 2021; L. Liu et al., 2024; Y. Liu et al., 2022). By measuring

strain changes along the wellbore, DSS allows estimates of fracture geometry while offering valuable insights into fracture behavior during injection and production from the geothermal reservoir (Jin et al., 2021; Leggett et al., 2022; Y. Liu et al., 2022).

This study proposes a strain transfer model to estimate fracture width from Rayleigh Frequency Shift Distributed Strain Sensing (RFS-DSS) field data. Our model adopts an existing strain transfer model originally used in concrete structures to address variations in elastic properties and interfacial slip within multilayer systems. We integrate this model with a linear elastic fracture model that considers rock strain resulting from its mechanical and elastic properties. The predicted fracture width from the proposed strain transfer model can be used to estimate the subsurface fluid circulation area using subsurface flow circulation volume data obtained from tracer tests. This information is essential for designing injection strategies that maintain continuous fluid circulation through the fractures, ensuring efficient thermal recovery and optimizing long-term reservoir performance. Figure 1a and 1b presents a schematic of a fiber cable installed in the producer-well of a geothermal reservoir showing the intermediate layers of the well completion system.

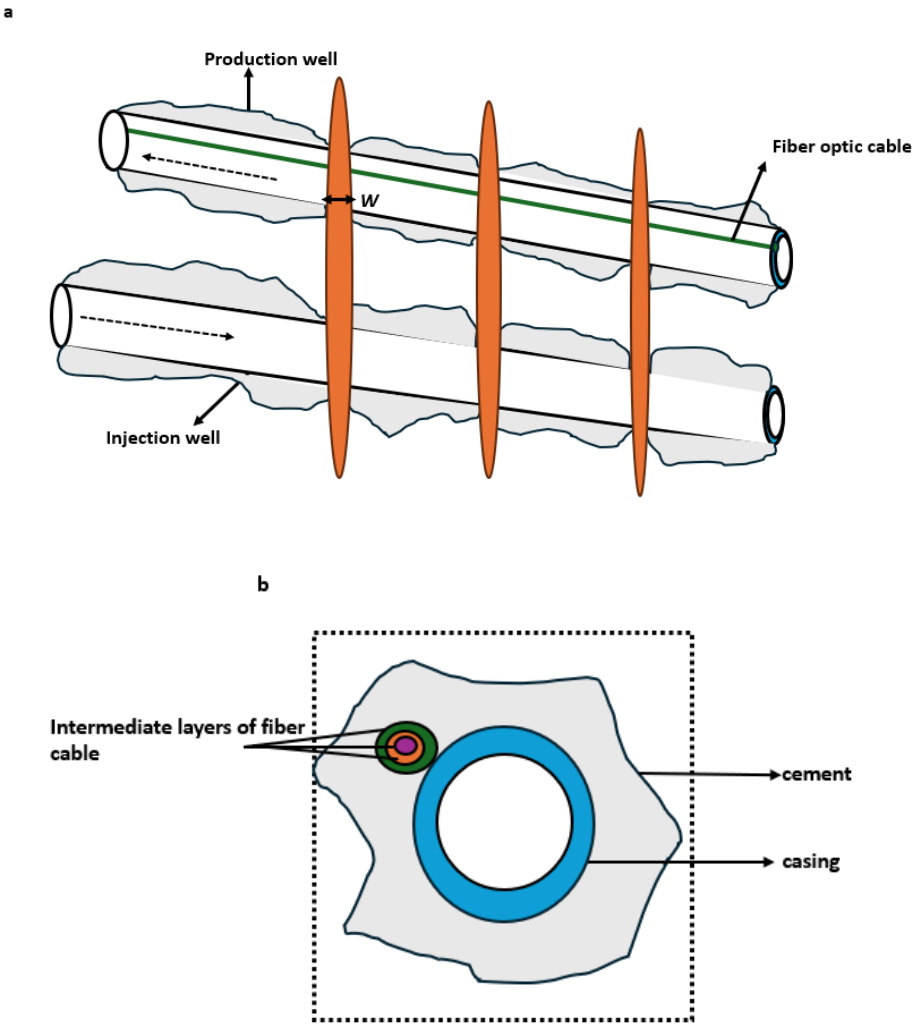


**Figure 1: (a) Schematic illustration of a fiber optic cable installed in the producer well of a geothermal reservoir. (b) Illustration of the intermediate layers of the well completion assembly in a geothermal reservoir.**

## 2. METHODOLOGY

In this work, we calculate the fracture width from RFS-DSS field data using a strain transfer model. To account for variations in the elastic properties of multilayer systems, we adopt the strain transfer model proposed by (Bassil et al., 2020) as described in Equation (2).

$$\varepsilon_f(z) = \lambda \frac{w}{2} e^{-\lambda|z|} + \varepsilon_{zz} \tag{2}$$

Where $\varepsilon_f(z)$ represents the axial strain along a fiber normal to the plane of a fracture, $w$ is the fracture width, $\varepsilon_{zz}$ is the rock strain, and $\lambda$ is the strain lag parameter, which can be determined using Equation (3).

$$\lambda^2 = \frac{2}{E_f r_f^2 \left[\frac{1}{G_1}\ln\left(\frac{r_1}{r_f}\right) + \sum_{i=2}^{N}\frac{1}{G_i}\ln\left(\frac{r_i}{r_{i-1}}\right) + \sum_{i=1}^{N}\frac{1}{k_i r_i}\right]} \quad (3)$$

Here, $E_f$ and $r_f$ denotes the Young's modulus and the radius of the fiber, respectively. G represents the shear modulus of the first layer in the multilayer system, $r_i$ is the radius of each layer and $k_i$ is the stiffness coefficient of each layer. The Bassil's equation offers a generalized approach to accounting for interfacial slip and differences in the elastic properties of multilayers systems with imperfect bonding. The main assumptions of Bassil's model are outlined below.

- Bassil assumes that the multilayer system is made up of a series of concentric layers surrounding an optical fiber at its center. The system is analyzed using cylindrical coordinates, denoted as (*r, θ, z*), with the z being the axial displacement of the fiber. The fiber coatings deform elastically under shear stress, and it is assumed that the radial displacements are minimal in comparison to the axial displacements.
- The interfacial slip between two intermediate layers in a multilayer system is directly proportional to the shear stress and inversely proportional to the stiffness parameter. However, this assumption might not be practical in all cases.
- The rock strain, $\varepsilon_{zz}$, varies linearly with the z direction. While this simplifies the analysis and enables practical application, it may not fully capture the nonlinear behavior of rock strain on either side of a fracture.

In this paper, we integrate Bassil's model with a linear elastic fracture model that accounts for the rock strain. The developed strain transfer model is applied to predict fracture width from RFS-DSS field data. The Bassil component of the strain transfer model is first utilized to estimate fracture width by performing a curve fit of the strain measurements in the exponential form described in Equation (4) to confirm with Bassil equation shown in Equation (2). The initial estimation of the fracture width using Equation (1) assumes that the rock strain, $\varepsilon_{zz}$ is zero, yielding Equation (5).

$$y = Ae^{-bx} \quad (4)$$

For this work, the strain-lag parameter will be obtained from the exponential curve fitting of the RFS-DSS strain data as described in Equation (4) above. This will further be illustrated in the results section of this paper. The initial estimation of the fracture width using Equation (2) assumes that the rock strain, $\varepsilon_{zz}$ is zero, yielding Equation (5).

$$\varepsilon_f(z) = \lambda\frac{w}{2}e^{-\lambda|z|} \quad (5)$$

The fracture width deduced from Bassil's model in Equation (1) is then equated to the width of the center of a penny-shaped fracture as described by (Sneddon et al., 1946) in Equation (6).

$$w = \frac{8P_{net}(1-v^2)c}{\pi E} \quad (6)$$

$P_{net}$ refers to an equivalent net pressure distributed over a fracture with radius "c", while E and v represents the young modulus and Poisson's ratio of the rock, respectively. Using Equation (6) above, the corresponding equivalent net pressure required to create a propped fracture width is determined. This equivalent net pressure is then used to calculate the normal displacement ($u_z$) along the fiber and subsequently the rock strain $\varepsilon_{zz}$ using Equations (7) and (8) respectively.

$$u_z = \frac{-4P_{net}c(1-v^2)}{\pi E}\int_0^\infty\left(1+\frac{\zeta\eta}{2(1-v)}\right)\left(\frac{\cos\eta}{\eta} - \frac{\sin\eta}{\eta^2}\right)e^{-\zeta\eta}J_0(\rho\eta)d\eta \quad (7)$$

$$\varepsilon_{zz} = \frac{d}{dz}\frac{-4P_{net}c(1-v^2)}{\pi E}\int_0^\infty\left(1+\frac{\zeta\eta}{2(1-v)}\right)\left(\frac{\cos\eta}{\eta} - \frac{\sin\eta}{\eta^2}\right)e^{-\zeta\eta}J_0(\rho\eta)d\eta \quad (8)$$

The terms $\zeta$ and $\rho$ can be described by Equations (9) and (10) below.

$$\zeta = \frac{z}{c} \quad (9)$$

$$\rho = \frac{r}{c} \quad (10)$$

Where $z$ denotes the distance from the fracture center and $r$ is the fiber radial offset between the treatment and monitor wells. Figure 2 describes the r and z coordinates of the fracture in a stimulated well.

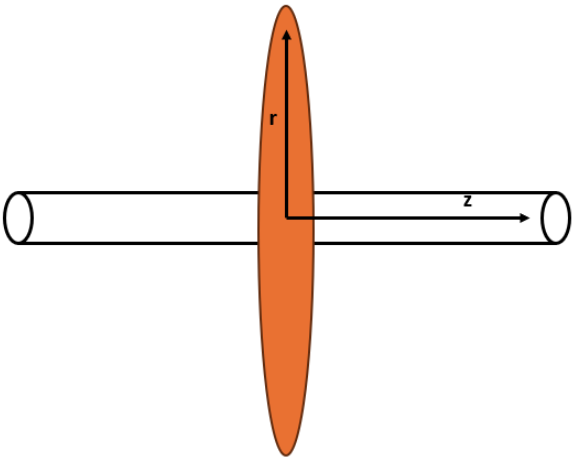


**Figure 2: Schematic showing the r and z coordinates of the fracture.**

The fiber radial offset, *r*, can be determined using Equation (11) below:

$$r_{offset}=\sqrt{\Delta h^2+\Delta l^2} \tag{21}$$

The terms, "*Δh"* and "*Δl"* represents the vertical and lateral offsets of the treatment and monitor wells, respectively. In this work, r is zero, as we consider a vertical, radial fracture centered around a horizontal wellbore instrumented with fiber. The modeled fiber strain is then computed using the developed strain transfer model in Equation (12).

$$\varepsilon_f=\lambda\frac{w}{2}e^{-\lambda|z|}+\frac{d}{dz}\frac{-4P_{net}c(1-v^2)}{\pi E}\int_0^{\infty}\left(1+\frac{\zeta\eta}{2(1-v)}\right)\left(\frac{\cos\eta}{\eta}-\frac{\sin\eta}{\eta^2}\right)e^{-\zeta\eta}J_0(\rho\eta)d\eta \tag{12}$$

The known fiber strain derived in Equation (1) from DSS field data is compared to the modeled fiber strain obtained from Equation (12). The predicted fracture width is then iterated until the known fiber strain correlates with the modeled fiber strain. The final fracture width obtained from the proposed strain transfer model represents the equivalent width of the propagated fracture after stimulation as analyzed from RFS-DSS field data. This fracture width can then be used to estimate the flow circulation area based on subsurface fluid circulation volume obtained from tracer tests using Equation (1). Figure 3 illustrates the developed strain transfer model, which integrates the Bassil and linear fracture models.

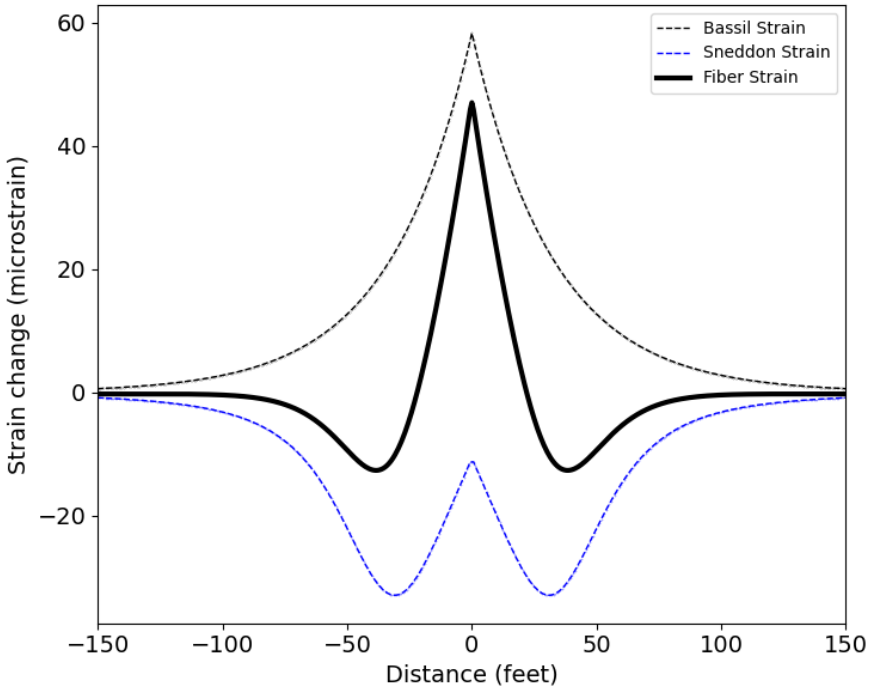


**Figure 3: Schematic of the developed strain transfer model.**

The workflow for applying the strain transfer model can be summarized as follows:

1. Obtain the strain-lag parameter by plotting the RFS-DSS strain data in the form of $y = Ae^{-bx}$.
2. Estimate the fracture width using Equation (1).
3. Equate the estimated fracture width to Sneddon's penny shaped width using Equation (3) and calculate the corresponding equivalent net pressure.
4. Using the calculated net pressure, determine the displacement along the fiber using Equation (4).
5. Calculate the rock strain using Equation (5).
6. Calculate the fiber strain using Equation (8) and compare the modeled strain with the strain obtained from the RFS-DSS data in Step 2.
7. Adjust the estimated fracture width until the modeled fiber strain aligns with the measured fiber strain from the RFS-DSS data.

## 3. RESULTS

To apply the proposed strain transfer model, we required a dataset with RFS-DSS measurements during pressure buildup and/or drawdown test. The tests conducted as part of the Hydraulic Fracture Test Site 2 (HFST2) project were used for this work (Jin et al., 2021). Figure 4 shows the RFS-DSS response to pressure buildup after shutting in a producer. These measurements have been interpreted according to the following logic. As pressure builds up in the fractures during a shut-in, a tensile strain registers on the portion of the fiber with productive fractures. Clusters that do not register a strain change likely do not contribute to production (Jin et al., 2021).

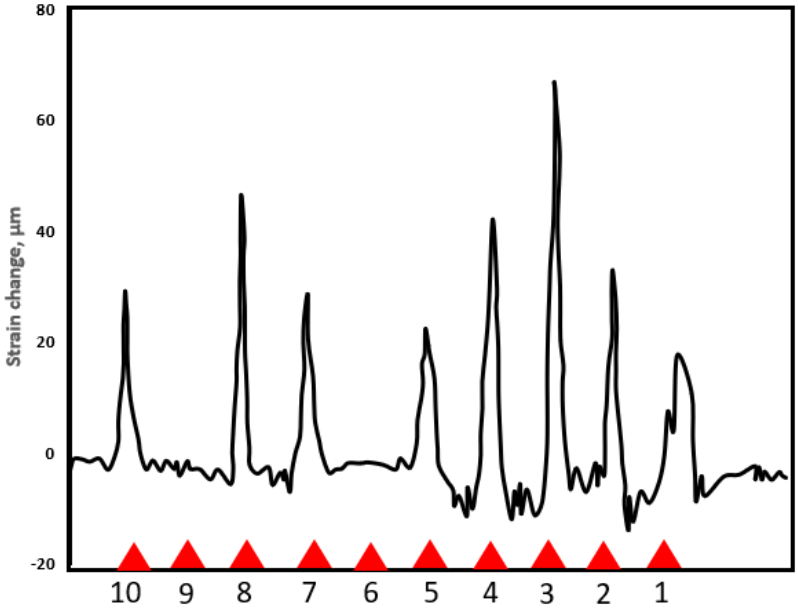


**Figure 4: Measured DSS response at different perforation clusters** (Jin et al., 2021).

We applied our strain transfer model to extract the fracture width of all the clusters in Figure 4 which were contributing to production. Following the methodology workflow described in the previous section, we plotted the strain data for each of the clusters in the exponential form described in Equation (4), in accordance with Bassil's model shown in Equation (2). The strain-lag parameter used for this work is derived from the equation of the exponential plot of the strain data. It accounts for the mechanical properties and interfacial slip between the intermediate layers of the well completion system. Figure 5 presents an example of the exponential plot of the strain data. The parameters used for the strain transfer modeling are shown in Table 1. The modeled clusters contributing to production are depicted in Figures 6 to 13.

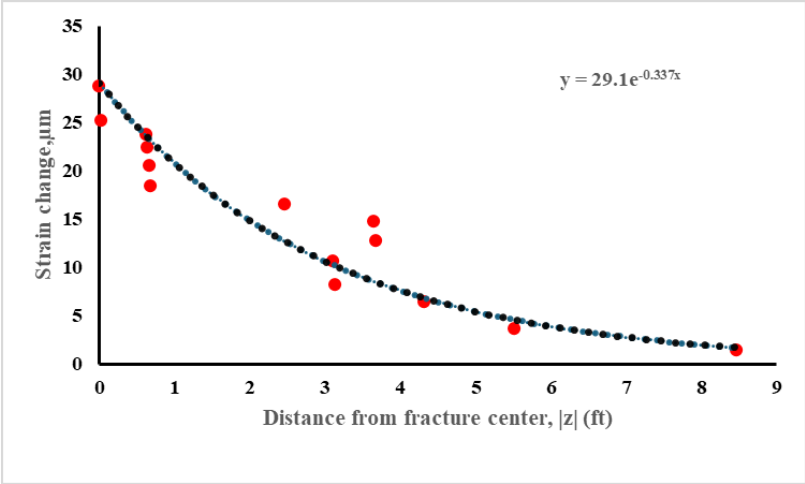


**Figure 5: Exponential curve fitting for cluster 7**

From the curve fit, the exponential coefficient leads us to an initial estimate of the strain lag parameter λ. Comparing Equation (5) and Figure 5, the strain lag parameter for cluster 7 is initially guessed as 0.337 1/ft. Subsequent improved curve fitting accounting for rock strain is conducted according to the method outlined above. This process is then applied for all the clusters to extract the fracture width from the RFS-DSS strain data. Key modeling parameters used are presented in Table 1. Note that the assumed fracture radius of 65 ft is small, but that it refers to an effective, propped, fracture radius. Figures 6 – 13 display the modeled and measured fiber strain for each cluster in Figure 4.

**Table 1: Modeling parameters for perforation clusters**

| Parameters | Values |
|---|---|
| Young's Modulus | 7.25 |
| Poisson's ratio | 0.25 |
| Effective fracture radius (ft) | 65 |
| Equivalent net pressure (psi) | 350-1180 |

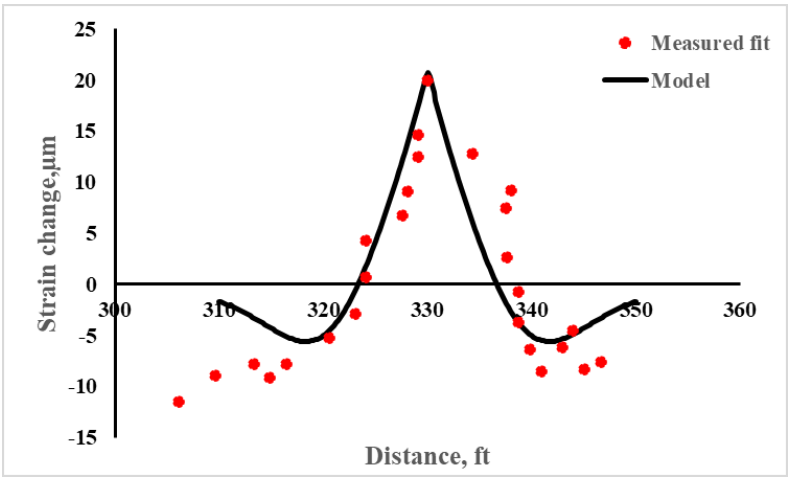


**Figure 6: Modeled and measured strain response for cluster 1**

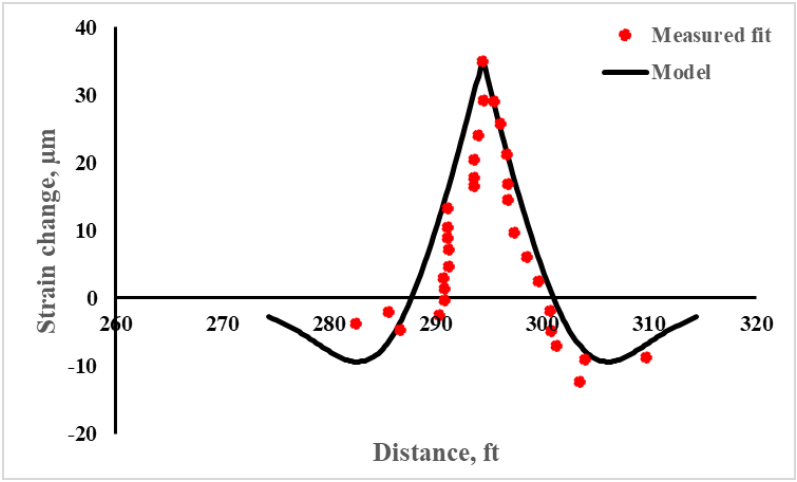


**Figure 7: Modeled and measured strain response for cluster 2**

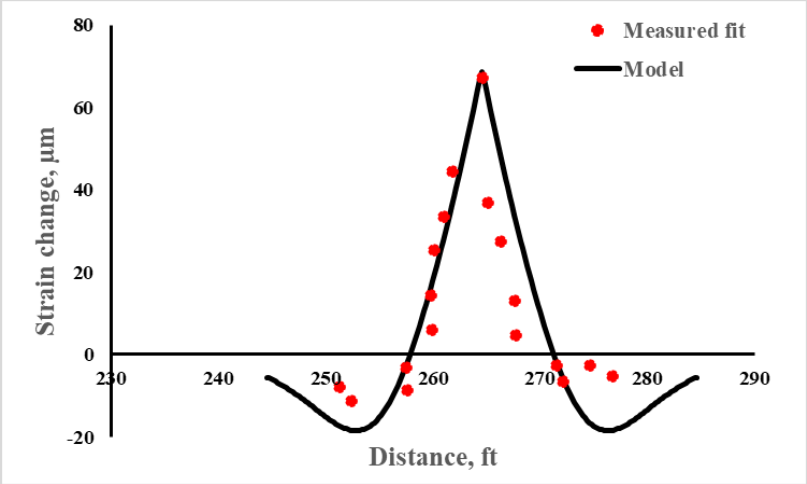


**Figure 8: Modeled and measured strain response for cluster 3**

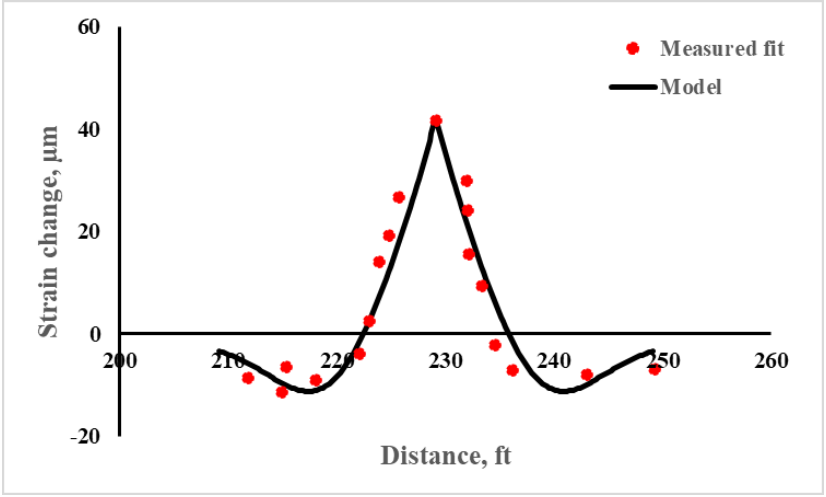


**Figure 9: Modeled and measured strain response for cluster 4**

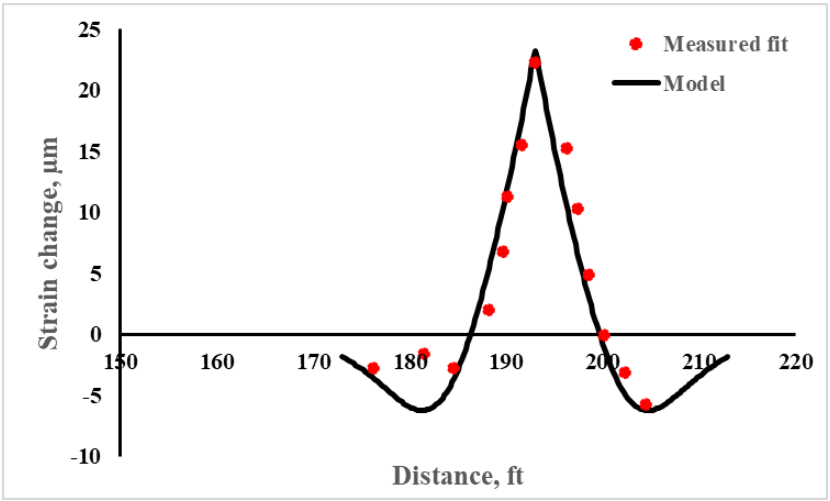


**Figure 10: Modeled and measured strain response for cluster 5**

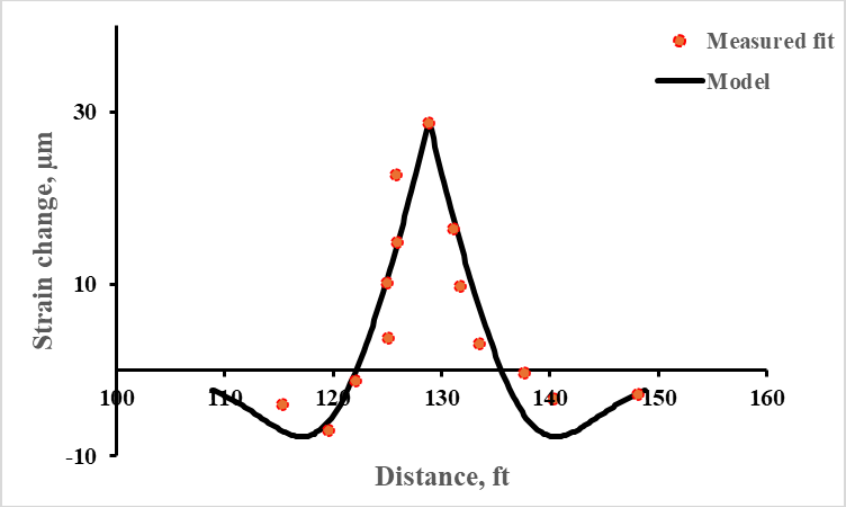


**Figure 11: Modeled and measured strain response for cluster 7**

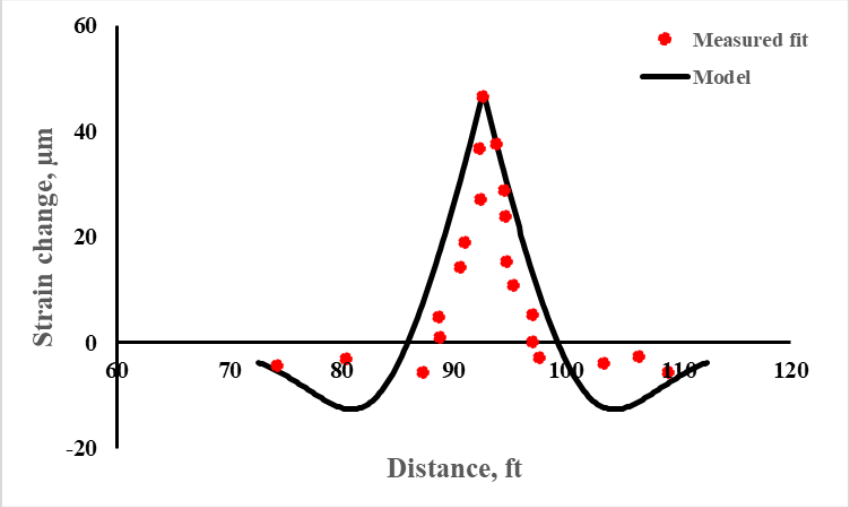


**Figure 12: Modeled and measured strain response for cluster 8**

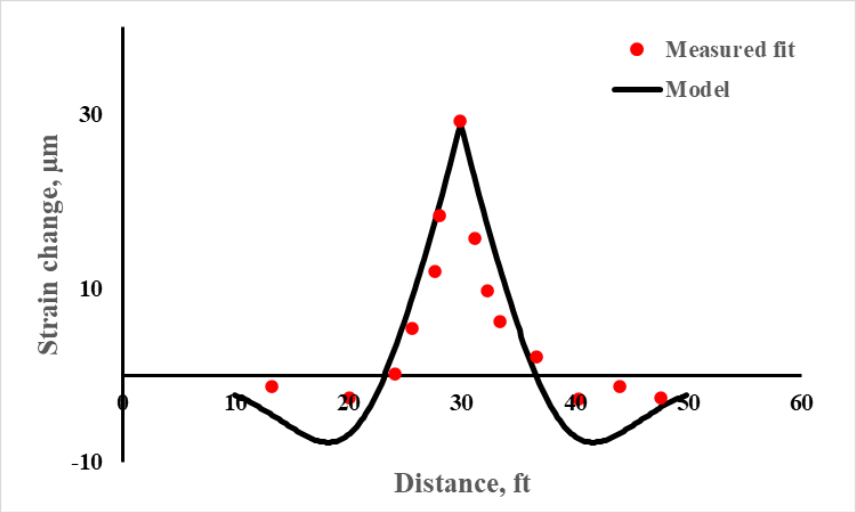


**Figure 13: Modeled and measured strain response for cluster 10**

The extracted fracture widths for all perforation clusters are presented in Table 2 below. The results, summarized in Figure 14, suggest a general correlation between the magnitude of the strain response and the propped fracture width. Clusters with higher tensile strain rates tend to have greater fracture widths. The response is not proportional because of different strain lag parameters at each cluster. The modeled strain lag parameters fall within a range of 0.18 – 0.59. A smaller strain lag parameter results in a wider, more broad region of tensile strain, and suggests weaker coupling between the fiber and formation than clusters with higher strain lag parameters. We observe the modeled strain lag parameter generally increases with fracture width in these modeled cases. We do not speculate on the reason for this, it may be coincidental.

**Table 2. Modeling Results Including Estimates of Fracture Width for Each Cluster**

| Clusters | Peak Measured Strain (µm) | Strain-lag (1/ft) | Predicted Fracture Width (in) | Equivalent Net Pressure (psi) |
|---|---|---|---|---|
| 1 | 20.07 | 0.184 | 0.08 | 354 |
| 2 | 34.91 | 0.552 | 0.13 | 366 |
| 3 | 68.57 | 0.571 | 0.2 | 1173 |
| 4 | 41.18 | 0.523 | 0.16 | 704 |
| 5 | 23.20 | 0.334 | 0.09 | 397 |
| 7 | 29.68 | 0.337 | 0.11 | 508 |
| 8 | 47.04 | 0.581 | 0.18 | 805 |
| 10 | 29.69 | 0.409 | 0.11 | 507 |

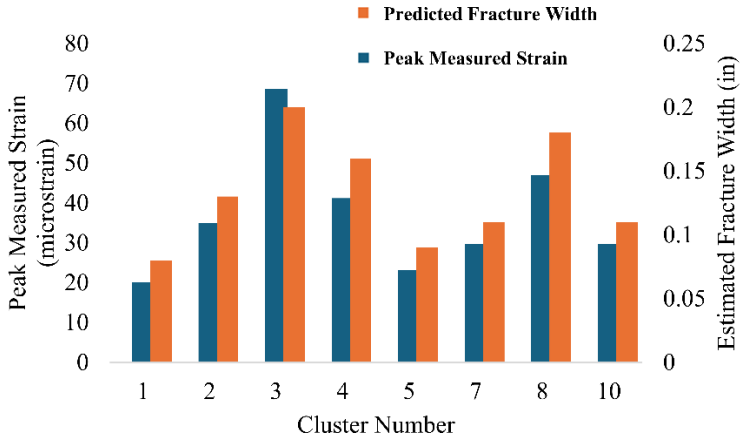


**Figure 14: The fracture width correlates with the peak measured strain for each cluster, but is not directly proportional.**

The fracture conductivity in Equation (13) is directly proportional to the fracture width.

$$C_f = k_f w_f \tag{33}$$

Here, $C_f$ is the fracture conductivity, $k_f$ represents the permeability of the fracture and $w_f$ denotes the fracture width.

The variation in predicted fracture widths across the different cluster as shown in Table 2 suggests that conductivity may differ significantly among them. Clusters with larger propped fracture widths such as Cluster 3 and 8 are expected to exhibit higher conductivity due to increased fracture aperture. Conversely, clusters with smaller fracture widths such as clusters 1 and 5 may have relatively lower conductivity due to their narrower apertures, even after proppant placement. The average predicted fracture width for all clusters is 0.13 in, which aligns with modeled results in other multistage fracture simulations (Mcclure et al., 2024). The fracture width, strain-lag parameter, and the mechanical and elastic properties of the rock all directly influence the tensile strain response observed during pressure

buildup. The proposed approach can be applied to predict the fracture width from RFS-DSS strain data obtained from flow circulation tests in geothermal reservoirs. When fluid is injected into the injection well of a geothermal reservoir, the bottom hole pressure increases, causing pre-existing fractures to reopen and propagate. This process is known as fracture recharge. The injected fluid generates tensile stresses in the rock, leading to a commensurate tensile strain response, which is observed by the RFS-DSS instrumented-producer well. By accurately estimating fracture width from RFS-DSS data, we can gain valuable insights into the flow circulation area, which is crucial for optimizing the reservoir performance and ensuring efficient geothermal energy production.

## 4. CONCLUSION

This work proposes a strain transfer model to predict the fracture width from RFS-DSS field data obtained from fluid circulation tests in geothermal reservoirs. The model builds upon an existing strain transfer model used in concrete structures to address interfacial slip and variations in the elastic properties of multilayer systems. We integrated this model with a linear elastic fracture model that accounts for the rock strain. This strain transfer model was applied to determine the fracture width of different perforation clusters using the RFS-DSS strain data obtained from the HFST-2 project in the Permian-Delaware basin. Our observations revealed that:

- Perforation clusters exhibiting higher tensile strain rates corresponded with wider fractures,
- The average predicted fracture width across all clusters is 0.13 inches, which aligns with existing literature.
- The developed model illustrates that fracture width, the strain-lag parameter, and rock mechanical properties significantly influence the strain distribution induced by geothermal fractures.
- The predicted fracture width from the strain transfer model can be used to estimate the subsurface fluid circulation area using subsurface flow circulation volume data obtained from tracer tests. Determining the flow circulation area is crucial for optimizing geothermal reservoir performance, as it directly affects heat extraction efficiency and long-term well productivity. This insight is vital for developing injection strategies that ensure continuous fluid circulation through the fractures, thereby enhancing thermal recovery and optimizing the overall performance of the reservoir.
- RFS-DSS estimates of fracture widths can be used for fracture conductivity monitoring.

## REFERENCES

Bassil, A., Chapeleau, X., Leduc, D., & Abraham, O. (2020). Concrete Crack Monitoring Using a Novel Strain Transfer Model for Distributed Fiber Optics Sensors. *Sensors 2020, Vol. 20, Page 2220*, *20*(8), 2220. https://doi.org/10.3390/S20082220

Belyadi, H., Fathi, E., & Belyadi, F. (2017). Numerical Simulation of Hydraulic Fracturing Propagation. *Hydraulic Fracturing in Unconventional Reservoirs*, 251–267. https://doi.org/10.1016/B978-0-12-849871-2.00015-0

Cipolla, C. L., Warpinski, N. R., Mayerhofer, M. J., Lolon, E. P., & Vincent, M. C. (2008). The Relationship Between Fracture Complexity, Reservoir Properties, and Fracture Treatment Design. *Proceedings - SPE Annual Technical Conference and Exhibition*, *4*, 2215–2239. https://doi.org/10.2118/115769-MS

Cipolla, C. L., Williams, M. J., Weng, X., Mack, M., & Maxwell, S. (2010). Hydraulic fracture monitoring to reservoir simulation: Maximizing value. *Proceedings - SPE Annual Technical Conference and Exhibition*, *2*, 1377–1402. https://doi.org/10.3997/2214-4609.20145655/CITE/REFWORKS

*GDR: Utah FORGE: RESMAN Well 16A(78)-32 and 16B(78)-32 Stimulation and Circulation Tracer Test Results - 2024*. (n.d.). Retrieved January 29, 2025, from https://gdr.openei.org/submissions/1703

Jin, G., Ugueto, G., Wojtaszek, M., Guzik, A., Jurick, D., & Kishida, K. (2021). Novel Near-Wellbore Fracture Diagnosis for Unconventional Wells Using High-Resolution Distributed Strain Sensing during Production. *SPE Journal*, *26*(05), 3255–3264. https://doi.org/10.2118/205394-PA

Jung, H., Sharma, M. M., Cramer, D. D., Oakes, S., & McClure, M. W. (2016). Re-examining interpretations of non-ideal behavior during diagnostic fracture injection tests. *Journal of Petroleum Science and Engineering*, *145*, 114–136. https://doi.org/10.1016/J.PETROL.2016.03.016

Le Calvez, J. H., Bennett, L., Tanner, K. V., Grant, W. D., Nutt, L., Jochen, V., Underhill, W., & Drew, J. (2005). Monitoring microseismic fracture development to optimize stimulation and production in aging fields. *The Leading Edge*, *24*(1), 72–75. https://doi.org/10.1190/1.1859705

Leggett, S., Kerr, E., Zhu, D., & Hill, D. (2022). Rapid Estimations of Dynamic Hydraulic Fracture Fronts From Cross-well Low-Frequency Distributed Acoustic Sensing Strain-Rate Measurements. *SPE/AAPG/SEG Unconventional Resources Technology Conference, URTC 2022*. https://doi.org/10.15530/URTEC-2022-3722728

Liu, L., Guo, X., & Wang, X. (2024). Integrated wellbore-reservoir-geomechanics modeling for enhanced interpretation of distributed fiber-optic strain sensing data in hydraulic-fracture analysis. *Journal of Rock Mechanics and Geotechnical Engineering*, *16*(8), 3136–3148. https://doi.org/10.1016/J.JRMGE.2023.09.027

Liu, Y., Jin, G., & Wu, K. (2022). New Insights on Characteristics of the Near-Wellbore Fractured Zone from Simulated High-Resolution Distributed Strain Sensing Data. *SPE Reservoir Evaluation and Engineering*, *25*(1), 99–112. https://doi.org/10.2118/208587-PA

Mahmoud, A., Gowida, A., Aljawad, M. S., Al-Ramadan, M., & Ibrahim, A. F. (2021). Advancement of Hydraulic Fracture Diagnostics in Unconventional Formations. *Geofluids*, *2021*(1), 4223858. https://doi.org/10.1155/2021/4223858

McCabe, W. J., Barry, B. J., & Manning, M. R. (1983). Radioactive tracers in geothermal underground water flow studies. *Geothermics*, *12*(2–3), 83–110. https://doi.org/10.1016/0375-6505(83)90020-2

Mcclure, M. W., Irvin, R., England, K., & Mclennan, J. (n.d.). *Numerical Modeling of Hydraulic Stimulation and Long-Term Fluid Circulation at the Utah FORGE Project*. Retrieved January 29, 2025, from www.resfrac.com

McClure Mark, W., Hojung, J., Cramer Dave, D., & Sharma Mukul, M. (2016). The fracture-compliance method for picking closure pressure from diagnostic fracture-injection tests. *SPE Journal*, *21*(4), 1321–1339. https://doi.org/10.2118/179725-PA

Ou, C., Liang, C., Li, Z., Luo, L., & Yang, X. (2022). 3D visualization of hydraulic fractures using micro-seismic monitoring: Methodology and application. *Petroleum*, *8*(1), 92–101. https://doi.org/10.1016/J.PETLM.2021.03.003

Rahman, M. K., Salim, M. M., & Rahman, M. M. (2012). Analytical modeling of non-darcy flow-induced conductivity damage in propped hydraulic fractures. *Journal of Energy Resources Technology, Transactions of the ASME*, *134*(4). https://doi.org/10.1115/1.4007658/372896

Redden, G., Stone, M., Wright, K. E., Mattson, E., Palmer, C. D., Rollins, H., Harrup, M., & Hull, L. C. (n.d.). TRACERS FOR CHARACTERIZING ENHANCED GEOTHERMAL SYSTEMS. *PROCEEDINGS, Thirty-Fifth Workshop on Geothermal Reservoir Engineering*.

Ren, Y., Kong, Y., Pang, Z., & Wang, J. (2023). A comprehensive review of tracer tests in enhanced geothermal systems. *Renewable and Sustainable Energy Reviews*, *182*, 113393. https://doi.org/10.1016/J.RSER.2023.113393

Shook, G. M., & Suzuki, A. (2017). Use of tracers and temperature to estimate fracture surface area for EGS reservoirs. *Geothermics*, *67*, 40–47. https://doi.org/10.1016/J.GEOTHERMICS.2016.12.006

Sneddon, I. N., Sneddon, & N., I. (1946). The Distribution of Stress in the Neighbourhood of a Crack in an Elastic Solid. *RSPSA*, *187*(1009), 229–260. https://doi.org/10.1098/RSPA.1946.0077

Suzuki, A., Ikhwanda, F., Yamaguchi, A., & Hashida, T. (2019). Estimations of Fracture Surface Area Using Tracer and Temperature Data in Geothermal Fields. *Geosciences 2019, Vol. 9, Page 425*, *9*(10), 425. https://doi.org/10.3390/GEOSCIENCES9100425

Wang, H. Y., & Sharma, M. M. (2018). Modeling of hydraulic fracture closure on proppants with proppant settling. *Journal of Petroleum Science and Engineering*, *171*, 636–645. https://doi.org/10.1016/J.PETROL.2018.07.067

Wilson, Z. A., & Landis, C. M. (2016). Phase-field modeling of hydraulic fracture. *Journal of the Mechanics and Physics of Solids*, *96*, 264–290. https://doi.org/10.1016/J.JMPS.2016.07.019